

Active Region Moss: Doppler Shifts from Hinode/EIS Observations

Durgesh Tripathi

Inter-University Centre for Astronomy and Astrophysics, Pune University Campus, Pune 411007, India

Helen E. Mason

Department of Applied Mathematics and Theoretical Physics, University of Cambridge, Wilberforce Road, Cambridge CB3 0WA, UK

James A. Klimchuk

NASA Goddard Space Flight Center, Greenbelt, MD 20771, USA

ABSTRACT

Studying the Doppler shifts and the temperature dependence of Doppler shifts in moss regions can help us understand the heating processes in the core of the active regions. In this paper we have used an active region observation recorded by the Extreme-ultraviolet Imaging Spectrometer (EIS) onboard Hinode on 12-Dec-2007 to measure the Doppler shifts in the moss regions. We have distinguished the moss regions from the rest of the active region by defining a low density cut-off as derived by Tripathi et al. (2010). We have carried out a very careful analysis of the EIS wavelength calibration based on the method described in Young, O'Dwyer and Mason (2012). For spectral lines having maximum sensitivity between $\log T = 5.85$ and $\log T = 6.25$ K, we find that the velocity distribution peaks at around 0 km s^{-1} with an estimated error of $4\text{--}5 \text{ km s}^{-1}$. The width of the distribution decreases with temperature. The mean of the distribution shows a blue shift which increases with increasing temperature and the distribution also shows asymmetries towards blue-shift. Comparing these results with observables predicted from different coronal heating models, we find that these results are consistent with both *steady* and *impulsive* heating scenarios. However, the fact that there are a significant number of pixels showing velocity amplitudes that exceed the uncertainty of 5 km s^{-1} is suggestive of impulsive heating. Clearly, further observational constraints are needed to distinguish between these two heating scenarios.

Subject headings: Sun: corona — Sun: atmosphere — Sun: transition region — Sun: UV radiation

1. Introduction

The problem of solar coronal heating has provided a major challenge since the discovery of the hot corona in 1940s. The solution remains elusive, in spite of major advances in theoretical modelling and observational capabilities in recent years. For an overview of our current understanding of this problem, the reader is referred to Klimchuk (2006).

Active regions are the brightest long-lived regions on the Sun and present an ideal target of opportunity for studying the coronal heating problem. Active regions are comprised of a diffuse component (Viall and Klimchuk 2011) and a variety of observationally discrete structures, including fan loops, warm loops, and hot core loops. The fan loops (only the legs are visible) are large structures at the edges of active regions, which are characterised by cool emission ($<1\text{MK}$), the warm loops are clearly defined at around 1MK , for example in Transition Region and Coronal Explorer (Handy et al. 1999, TRACE), 173 \AA images (e.g. Del Zanna and Mason 2003) and the hot loops are seen in higher temperatures emission (3MK) for example in X-rays (with Hinode/XRT and Yohkoh/SXT). The moss emission, also clearly seen in TRACE 173 \AA , is believed to be the footpoints of the hot core loops (e.g. Tripathi et al. 2010, and references therein).

One of the main concerns regarding the coronal heating problem is whether all the different structures are heated via the same mechanism or whether there are different processes at work for different structures.

The observed properties of warm loops appear to be consistent with models of *multi-stranded loops* heated by low-frequency nanoflares (nanoflares with repetition time lags longer than a cooling time on each strand) (see e.g., Warren, Winebarger, and Mariska 2003; Tripathi et al. 2009; Ugarte-Urra, Warren, Brooks 2009; Klimchuk 2009, and references therein). However, the results for the hot core loops have not converged. There is compelling observational evidence for both steady heating (see e.g., Warren et al. 2008; Brooks and Warren 2009; Warren et al. 2010; Tripathi et al. 2010; Winebarger et al. 2011) as well as impulsive heating (Tripathi, Mason and Klimchuk 2010; Tripathi, Klimchuk and Mason 2011; Viall and Klimchuk 2012). Since it is not easy to observe the hot core loops directly, due to their inherent fuzzy nature (Tripathi et al. 2009; Guarrasi, Reale, Peres 2010), authors have focussed on studying the characteristics and dynamics of the moss regions (see e.g. Tripathi et al. 2010, and references therein). The moss regions provide important constraints on the heating of the hot core loops (e.g. Winebarger, Warren, Falconer 2008; Warren et al. 2010; Tripathi et al. 2010). One of the main arguments for steady heating is the minimal variability observed in the brightness of the moss emission (Antiochos et al. 2003), Doppler shifts, line widths (Brooks and Warren 2009) and electron density & temperature structure (Tripathi et al. 2010). However, we have argued that this can be uniquely interpreted only

if the plasma does not have unresolved structures (Tripathi, Mason and Klimchuk 2010).

One of the main hindrances to solving the coronal heating problem is that we are still far from resolving the fundamental structures in the solar corona (e.g. Klimchuk 2006; Warren et al. 2008; Tripathi et al. 2009; Tripathi et al. 2010; Young, O’Dwyer and Mason 2012). Therefore, the observationally derived properties of coronal structures relate to an ensemble of structures, rather than a fundamental structure itself. This could have severe consequences for the interpretation of the data. For example any small scale variations taking place in the fundamental structures could be completely washed out/averaged in our present day observations. Therefore, we have to rely on the diagnostic techniques which do not require the fundamental structures to be resolved. There are two main diagnostic methods for this purpose, the first being the emission measure (EM) distribution and the second being the Doppler shift of the plasma in the coronal structures. A third method involving time-lag analysis has recently been developed (Viall and Klimchuk 2012).

In this work we have made use of the Doppler shift techniques and studied the bulk flow of plasma in the moss regions, as advocated by Tripathi, Mason and Klimchuk (2010). This is potentially a powerful diagnostic tool to distinguish between steady heating and impulsive heating models. Models advocating steady heating in symmetric loops predict no Doppler shift because the loops are in a static equilibrium where heating, radiation, and thermal conduction are perfectly balanced. Asymmetries in the heating and/or cross sectional area will generate steady flows (e.g., Mariska and Boris 1983), but these flows will be slow unless the asymmetries are extreme (Winebarger et al. 2002; Patsourakos and Klimchuk 2004). Furthermore, the flows are end-to-end and produce blue shifts in one leg and red shifts in the other. Flows can also be generated in symmetric loops if the heating is very highly concentrated at the loop footpoints (e.g. Klimchuk, Karpen and Antiochos 2010; Lionello et al. 2012). These flows occur because of thermal nonequilibrium and are time-dependent even though the heating is steady.

Impulsive heating produces a very different Doppler shift signature. The standard picture envisions a collection of unresolved strands that are heating quasi-randomly by nanoflares (see e.g., Cargill 1994). An observed emission line then represents the combined emission from many out-of-phase strands. Upflows are generated by chromospheric evaporation, but these tend to be faint because the evaporation phase is short lived and because the initial densities are low. Downflows associated with the subsequent slow cooling and draining of the evaporated plasma tend to be brighter and therefore to dominate the emission. The composite line profile is therefore predicted to be a red-shifted core with an enhanced blue wing (Patsourakos and Klimchuk 2006). The Doppler shift that would be measured from a Gaussian fit will depend on the relative strengths of the upflow and

downflow emission. These change depending on the temperature of the emission line.

One goal of our study is to determine how Doppler shift depends on temperature. Constant mass flux at constant pressure implies that $v \propto T$. While we expect this relationship to hold on each strand at each moment in time, the relationship between Doppler shift and temperature for an unresolved collection of strands is not straightforward. Our preliminary modeling suggests that coronal nanoflares produce red shifts which decrease with temperature and eventually give way to blue shifts in hot lines (Bradshaw and Klimchuk, in preparation). The temperature of the transition depends on the strength of the nanoflares.

Hansteen et al. (2010) have proposed a different impulsive heating scenario. They suggest that nanoflares occurring in the upper chromosphere cause material to expand downward and upward away from the locally enhanced pressure. This produces red shifts in transition region emissions and blue shifts in coronal emissions.

Brooks and Warren (2009) studied the Doppler shift and non-thermal width and their temporal variation in moss regions using the Fe XII $\lambda 195$ line observed by the EIS. They reported a minimal red-shift of about 2-3 km s⁻¹ and almost no variability in Doppler shift and non-thermal width with time. These results led them to conclude that the hot core loops are heated in steady fashion. However, it is worthwhile mentioning here that the reference wavelength they choose for Doppler measurements was averaged over the complete raster. If the emission outside the core has a non-zero absolute Doppler shift, the red shifts reported for the core need to be adjusted up or down.

In the present paper we have made use of a more reliable method of EIS wavelength calibration developed by Young, O’Dwyer and Mason (2012). This is based on deriving velocities using Fe VIII in the quiet Sun region of each slit position in the raster. We consider our method, following that of Young, O’Dwyer and Mason (2012) to be much more robust than that used by Brooks and Warren (2009). The rest of the paper is organised as follows: in section 2 we describe the observation used in this study; in section 3 we have described the data analysis and results followed in section 4 by a discussion of results and conclusions.

2. Observations

The Extreme-ultraviolet Imaging Spectrometer (EIS; Culhane et al. 2007) onboard Hinode observed an active region, *AR 10978*, on 12-Dec-2007 (near the central meridian of the Sun) using the observing sequence *AR_velocity_map_v2*. This sequence uses the 1" slit with an exposure time of 40 seconds. The EIS raster used in this analysis started at 11:43 UT and was completed at 17:02 UT. The left image in Fig. 1 displays a full disk image recorded

by the Extreme-ultraviolet Imaging Telescope (EIT; Delaboudinière et al. 1995) onboard the Solar and Heliospheric Observatory (SOHO). The over-plotted box shows the area which was rastered by EIS, for which a spectral image built in Fe XII λ 195 is shown in the right panel.

This active region raster is ideal for a study of Doppler shifts since it is very close to the central meridian and it did not show any flaring/micro-flaring activity during the raster (as well a few days before and after the time of the observations) as shown by the GOES plots in Fig. 2. The location near the central meridian is important because any small flows, which are in the line-of-sight (LOS) can be detected with higher accuracy. It should be noted that the quiescence of the active region ensures that our measurements are not affected by any small scale dynamic features, such as micro-flares, occurring in the core of the active region.

The EIS study sequence used for this work comprises many different spectral lines. However, in this work we are only concerned with the Doppler shift in the moss regions and the temperature dependence of the Doppler shifts, so we have selected the subset of the spectral lines from the study, given in Table 1. The wavelengths shown in the second column in the table are adopted from Warren et al. (2011). Additionally, we have only used the spectral lines for our study which are cooler than Fe XIII, since the moss emission above this temperature is highly contaminated with overlying hot core loops, as was shown by Tripathi et al. (2008); Tripathi et al. (2010). It should be noted that since we are only interested in measuring the Doppler shift in the core of the active region, we have only used the exposures covering the core of the active region.

Table 1: Spectral lines used to study the the Doppler shift in the moss regions. The wavelengths shown in the second column are taken from Warren et al. (2011).

Ion Name	Wavelength (\AA)	$\log T_{max}$ (K)
Fe VIII	186.6060	5.60
Fe IX	197.8570	5.85
Fe X	184.5341	6.05
Fe XI	188.3940	6.15
Fe XII	195.1186	6.20
Fe XIII	202.0486	6.25

3. Data Analysis and Results

We have generated intensity and Doppler maps of the active region in the spectral lines listed in Table 1. As is well known, there are two instrumental effects with EIS (cf Young, O’Dwyer and Mason 2012), namely the orbital variation of the spacecraft and the tilt of the slits with respect to the detector. It is very important to allow for these when determining Doppler measurements. Whilst the tilt of the slits has been measured using independent observations and can be accounted for uniquely from the observations, removing the orbital variation is a non-trivial and non-unique process.

While deriving the Doppler maps, there is one additional very important matter, that of choosing a reference wavelength. In order to measure absolute line-of-sight velocity, we require a reference spectrum where the Doppler shift of the line is well known. Neutral or singly ionised photospheric or chromospheric spectral lines can be used to measure the absolute shift, as was demonstrated by Hassler et al. (1992) using a rocket based spectrometer with an onboard calibration lamp. This method is routinely used on Solar Ultraviolet Measurements of Emitted Radiation (SUMER; Wilhelm et al. 1995) observations (see e.g. Winebarger et al. 2002). Unfortunately this is not possible with the EIS spectrum since there are no spectral lines from neutral or singly ionized ions, with the exception of He II 304 which is problematic. Young, O’Dwyer and Mason (2012) developed a method whereby they used Fe VIII line in the Quiet Sun region to obtain the orbital variation and reference wavelength. We have also used this method and the Fe VIII $\lambda 186.6$ line in the Quiet Sun to derive the absolute wavelength for other lines. It is then necessary to establish the Doppler shift for the Fe VIII $\lambda 186.6$ line in the Quiet Sun.

Brooks, Warren and Young (2011) showed that although the ionisation equilibrium calculation suggests that the formation temperature of Fe VIII line is $\log T = 5.6$, the structures seen in Fe VIII intensity maps show more resemblance with structures seen at $\log T = 5.8$. This fortuitously matches with Ne VIII line for which absolute shift can be measured using SUMER observations.

Using SUMER measurements of the Quiet Sun, Peter and Judge (1999) found that Ne VIII line formed at $\log T = 5.8$ are blue-shifted by 2-3 km s^{-1} . On the other hand, Brekke, Hassler and Wilhelm (1997) and Chae, Yun and Poland (1998) found that this line was red-shifted by 5-6 km s^{-1} . In a recent paper, Dadashi, Teriaca and Solanki (2011) showed that the shift was zero at $\log T = 5.8$. However, we note that the velocity given in their plot at $\log T = 5.8$ is not an observational finding, but comes from three-dimensional MHD simulations by Hansteen et al. (2010). These measurements clearly suggest that there are large uncertainties in absolute velocity measurements at $\log T = 5.8$. Therefore, although Young, O’Dwyer and Mason (2012) used the Peter and Judge (1999) values in their mea-

surements, we have used zero shift at $\log T = 5.8$, consistent with Dadashi, Teriaca and Solanki (2011).

We note here that the Fe VIII $\lambda 186.6$ line is blended with Ca XIV $\lambda 186.61$ formed at $\log T = 6.5$ (Young et al. 2007). While this line may have a significant blend in the core of the active region, it has a negligible contribution when observing in the Quiet Sun. Therefore, this line can safely be used to derive orbital variation and rest wavelength. The method used can be briefly described as follows: we first identified the lower part of the Fe VIII raster as Quiet Sun and binned the data in y-direction by 40 pixels (Figure 3). This increases the signal to noise ratio quite significantly. These bottom 40 pixels have intensities equivalent to the quiet Sun intensities derived by Brooks et al. (2009). We used these binned Quiet Sun data to get orbital variation of the spacecraft and rest wavelength for Fe VIII line. Using the off-limb observations of Warren et al. (2011), and assuming that the absolute Doppler shifts vanish for these off limb locations, we know the rest separation of all the other lines with respect to the Fe VIII $\lambda 186.6$ line. This separation is used to retrieve absolute wavelengths for all the other lines used in this study. Using this method, Young, O’Dwyer and Mason (2012) found that velocities can be measured with an accuracy of 4–5 km s⁻¹.

Figures 3 & 4 display intensity and velocity maps for the active region in the chosen spectral lines mentioned in Table 1. The overall intensity structures and Doppler shift patterns are similar to those derived by previous authors, i.e., red-shifted loop structures (around 1MK) with blue-shifted hotter regions at the boundary of the active regions (see e.g. Doschek et al. 2008; Del Zanna 2008; Marsch et al. 2008; Tripathi et al. 2009). In addition, as also shown by Tripathi et al. (2009), the footpoints of the loops are highly red-shifted at transition region temperatures with the magnitude of the flow decreasing with rising temperature (see also Del Zanna 2008). As can also be seen from the figures, the blue shifts at the boundary of the active region increase with temperature.

As noted out earlier, Fe VIII $\lambda 186.6$ is blended with Ca XIV $\lambda 186.61$ which is formed at $\log T = 6.5$. The Ca XIV $\lambda 186.61$ line has a constant branching ratio of 0.7 with the Ca XIV $\lambda 193.8$. Therefore, if Ca XIV $\lambda 193.8$ is observed in the spectrum, the contribution of Ca XIV $\lambda 186.61$ can be estimated. Unfortunately, in this study sequence, Ca XIV $\lambda 193.8$ was not observed. However, analysing the moss and inter-moss spectra for another active region studied by Tripathi, Mason and Klimchuk (2010) and Tripathi, Klimchuk and Mason (2011), we find that the contribution of the Ca XIV $\lambda 186.61$ line could be as high as 20–25% in moss regions and about 50% in the inter-moss regions. Therefore, the intensity map for Fe VIII $\lambda 186.6$ shown in the top left panel of Fig. 3 may have significant contribution due to Ca XIV $\lambda 186.61$ in the core of the active region. Hence, it is plausible to conclude that the red-shifts which are seen corresponding to the Fe VIII line is likely to be over-estimated

in the core of the active region. By performing a simple analytical calculation we find that if the peak of Ca XIV $\lambda 186.61$ is 20% of that of Fe VIII $\lambda 186.6$, the overestimation in the redshift would be of 3.8 km s^{-1} . However, if the peak of Ca XIV $\lambda 186.61$ is 50% of that of Fe VIII $\lambda 186.6$, then the overestimation could be as large as 6.8 km s^{-1} .

The identification of the moss regions is not uniquely defined. Usually moss regions are visually identified based on the high spatial resolution observations recorded by TRACE in its 173 Å band, which is sensitive to Fe IX and Fe X emission at around 1MK. Unfortunately, there were no TRACE observations for this active region. Although there are EIT 171 observations essentially showing the same emission as TRACE 173, the spatial resolution is not adequate to identify moss regions unambiguously. Therefore, we have to rely on EIS observations. Warren et al. (2008) identified moss regions using an intensity threshold for the Fe XII $\lambda 186.8$ line intensity, which is sensitive to electron density. We follow a similar approach.

Tripathi et al. (2010) studied the density structure in different moss regions and found that the electron densities are greater or equal to $2 \times 10^9 \text{ cm}^{-3}$ (derived using Fe XIII line ratio). In this EIS study, we have two density sensitive lines of Fe XIII, namely $\lambda 202.04$ and $\lambda 203.82$, which could be used to derive density map of the active region.

It has been found that the two CCDs of EIS are not exactly aligned with each other (Young et al. 2007). Since the lines we have used in this study are all from the sort-wavelength band, this effect does not apply here. However, due to slight misalignment between the dispersion axis of the grating and the axis of the CCD, the images show small Y-offset (Young et al. 2009). We have accounted for the Y-offset between different lines using standard post processing routines provides in *SSWIDL*.

Fig. 5 displays the intensity maps obtained in Fe XIII $\lambda 202.04$ (left panel) and $\lambda 203.82$ (middle panel) and the corresponding density map (right panel) derived from the ratio of these lines. The density maps are derived using the CHIANTI v6.1 (Dere et al. 1997, 2009) atomic database. As can be seen from the intensity and density maps, the moss regions are the densest regions in the map. However, to uniquely obtain the locations of moss regions, we have used the electron densities in moss regions derived by Tripathi et al. (2010) to determine a cut-off in electron density. We have displayed the density map with $\log N_e \geq 9.3$ in Fig. 6. We believe that these cut-off values for density uniquely distinguish the moss region from other parts of the active region raster. We continue to study the Doppler shift in those pixels only. It is important to emphasize that when extending the moss regions identified using densities derived using Fe XIII ratios to other lines, it is very important to account for the Y-offset between different lines. We have allowed for this effect in our analysis.

Figure 7 displays the histograms of the Doppler shift for the pixels with densities with $\log N_e \geq 9.3$ (shown in Fig. 6) for all the spectral lines listed in Table 1. As can be very clearly seen, all the histogram plots peak very close to zero on the negative velocity (blue) side, with the exception of the Fe VIII line (which is blended with the Ca XIV line). We note here, however, that if we assume that contribution of Ca XIV is as high as 20% and subtract 4 km s^{-1} from the Fe VIII velocity histogram, the histogram will peak at around 5 km s^{-1} . This is similar to what is found in Ne VIII, which forms almost at the same temperature to that of Fe VIII, observed in Moss regions using SUMER spectra (Winebarger et al. in preparation). The velocity distribution for all other lines peaks close to zero. With increasing temperature, the histogram starts to become asymmetric with more points on the blue side. Table 2 provides the mean, median and standard deviation values of the measured velocity distributions for all the lines in the moss region. The absolute mean velocities are negative i.e. blue shift, which is increasing with temperature. We have also computed the second moment of the velocity distribution i.e. standard deviation given in the 5th column of the table. The standard deviation decreases with temperature. Since the mean and median of the measured velocity distributions were within the systematic errors on the measurements, we wanted to find out how many moss pixels have definite shifts. For this purpose we computed the fraction of pixels with velocity amplitudes greater than the 5 km s^{-1} uncertainty (shown in the 2nd to last column of the Table 2). We can also take the highly conservative view that the absolute velocity calibration is unknown. In that case, the fraction of pixels that deviate from the mean by more than the 5 km s^{-1} uncertainty (last column in the table) is the smallest possible fraction of pixels that must have a non-zero Doppler shift. The subscript 'i' represents the moss pixels. Both of these measures indicate that a sizable fraction of moss pixels ($\approx 30\%$ for Fe IX) cannot be at rest.

It is worthwhile mentioning that there may be a few pixels qualifying as moss (based on the density cut-off definition) affected by the tilted point spread function of EIS (see e.g.. Young, O'Dwyer and Mason 2012; Scott and Martens 2012; Tripathi, Mason and Del Zanna 2012). Due to this effect, the intensity and corresponding velocity signatures may be shifted by 1 pixel when there is a sharp change in intensity. Therefore, although the pixel in the intensity map fulfils the criteria of moss, the velocity signature of that pixel would be moved to another adjacent pixel which may not fulfil the criteria.

4. Summary and Discussion

We have studied the Doppler shift and temperature dependence of the Doppler shift in moss regions using an active region observation recorded on 12-Dec-2007. We have distin-

guished the moss regions from the rest of the active region by defining a low density cut-off as was derived by Tripathi et al. (2010). The histograms of the velocity distributions peak at around 0 km s^{-1} . This is true for all the spectral lines studied in this work, except the Fe VIII line which is blended with a Ca XIV line in its red-wing leading to unreliable results in the active region core. The mean of the distributions show blue shifts which increase with temperature. With increasing temperature, the width of the distribution decreases and the distribution becomes asymmetric towards the blue. In addition, there are significant number of pixels showing velocities larger than the error i.e. 5 km s^{-1} shown the last two columns of Table 2.

Using analytical modeling, Bradshaw (2008) suggested that the radiation from moss regions is powered by an enthalpy flux from cooling and draining of coronal plasma. He predicted that downflow speeds at $T = 1 \text{ MK}$ ranging between 2.9 and 3.4 km s^{-1} should be observed. We observe Doppler shifts close to zero. However, we note that we have a large uncertainty of about $4\text{-}5 \text{ km s}^{-1}$ in our measurements. The observed line profiles are a composite made up of red-shifted emission from a cooling downflow and faster blue-shifted emission from either evaporating plasma associated with nanoflares (Patsourakos and Klimchuk 2006) or hot plasma at the tips of Type-II spicules (De Pontieu et al. 2011). The analysis of Bradshaw (2008) applies only to the dominant red-shift component. As the blue-shift component becomes progressively brighter, as predicted for higher temperatures (Patsourakos and Klimchuk 2006), it will displace a Gaussian fit of the line profile further to the blue, consistent with our findings. Further work is in progress relating to this effect, using models with nonequilibrium ionization (Bradshaw and Klimchuk 2011).

There have been some previous measurements of Doppler shifts in moss regions. Klimchuk (1987) found that active region plage (essentially an early term for moss) are red shifted by approximately $10\text{-}15 \text{ km s}^{-1}$ in the C IV $\lambda 1548$ line formed at 0.1 MK . This is consistent with the picture that red shifts are strongest at low temperatures and become progressively weaker at higher temperatures, eventually transitioning to blue shifts. Our observations appear to bracket this range of transition. The trend from red shift to blue shift with increasing temperature has been reported previously for the quiet Sun (Peter and Judge 1999), and it is now clear that it also applies to active region moss. However, the transition from red to blue appears to occur at a higher temperature in moss ($\approx 1 \text{ MK}$ versus 0.5 MK in the quiet Sun). Our preliminary modeling results suggest that this can be explained by higher energy nanoflares in active regions (Bradshaw and Klimchuk, in preparation).

Although our results are consistent with impulsive heating model, we cannot rule-out steady state heating scenario, where conductive flux from the corona is balanced by radiative cooling. This basically suggests no bulk flow i.e. 0 km s^{-1} (although see e.g.,

Mariska and Boris 1983), which is consistent with what we observe in this paper for the peak of the velocity distribution. However, we also observe apparent asymmetries in the distribution with increasing temperature, which is not predicted from the steady heating scenario. It is worthwhile noting here that our uncertainties in the absolute velocities are so large ($4\text{--}5 \text{ km s}^{-1}$) that we cannot rule-out one model against other for most pixels, solely based on the Doppler shift measurements using EIS data. However, the result that there are significant number of pixels with velocity amplitudes larger than 5 km s^{-1} indicates that the heating is not steady at those locations and may suggest that impulsive heating is more likely in general.

Further, more accurate measurements of Doppler shifts in moss regions are urgently required to distinguish between the different heating scenarios. We note that NASA's Interface Region Imaging Spectrometer (IRIS) is to be launched in late 2012 and should provide some conclusive results, in particular if IRIS observations are combined with EIS studies of moss regions. In addition, ESA's Solar Orbiter is to be launched in 2017 and the planned Solar-C mission will provide unprecedented opportunities to perform such Doppler shift measurements with higher accuracy.

We thank an anonymous referee for constructive comments which has improved the paper. We acknowledge useful discussions at the ISSI on Active Region Heating. We also acknowledge the loops workshops as an opportunity to stimulate discussions and collaborate on this project. HEM acknowledges support from STFC and JAK acknowledges support from the NASA Supporting Research and Technology Program. We thank Dr Peter Young for various discussions. Hinode is a Japanese mission developed and launched by ISAS/JAXA, collaborating with NAOJ as a domestic partner, NASA and STFC (UK) as international partners. Scientific operation of the Hinode mission is conducted by the Hinode science team organised at ISAS/JAXA. This team mainly consists of scientists from institutes in the partner countries. Support for the post-launch operation is provided by JAXA and NAOJ (Japan), STFC (U.K.), NASA, ESA, and NSC (Norway). CHIANTI is a collaborative project involving researchers at NRL (USA) RAL (UK), and the Universities of: Cambridge (UK), George Mason (USA), and Florence (Italy).

REFERENCES

- Antiochos, S. K., et al. 2003, ApJ, 590, 547
Bradshaw, S. 2008, A&A, 486, L5

- Bradshaw, S., and Klimchuk, J. A. 2011, *ApJS*, 194, 26
- Brekke, P., Hassler, D. M., and Wilhelm, K. 1997, *Sol. Phys.*, 175, 349
- Chae, J., Yun, H. S., and Poland, A. I. 1998, *ApJS*, 114, 151
- Brooks, D. H. and Warren, H. P. 2009, *ApJ*, 703, 10
- Brooks, D. H., Warren, H. P., Williams, D. R., Watanabe, T. 2009, *ApJ*, 705, 1522
- Brooks, D. H., Warren, H. P. and Young, P. R. 2011, *ApJ*, 730, 85
- Brown, C. M., Feldman, U., Seely, J. F., Korendyke, C. M., and Hara, H. 2008, *ApJS*, 176, 511
- Cargill, P. J. 1994, *ApJ*, 422, 381
- Chae, J., Yun, H. S., and Poland, A. I. 1998, *ApJS*, 114, 151
- Culhane, J. L., et al. 2007, *Sol. Phys.*, 243, 19
- Dadashi, N., Teriaca, L., and Solanki, S. K., 2011, *A&A*, 534, 90
- Del Zanna, G. 2008, *A&A*, 481, L49
- Del Zanna, G., Mason, H. E. 2003, *A&A*, 406, 1089
- Delaboudinière, J.-P., Artzner, G. E., Brunaud, J. et al. 1995, *Sol. Phys.*, 162, 291
- De Pontieu, B., et al. 2011, *Science*, 331, 55
- Dere, K. P., Landi, E., Mason, H. E., Monsignori Fossi, B. C. and Young, P. R. 1997, *A&AS*, 125, 149
- Dere, K. P., Landi, E., Young, P. R., Del Zanna, G., Landini, M. and Mason, H. E. 2009, *A&A*, 498, 915
- Doschek G. A. et al. 2008, *ApJ*, 682, 1362
- Guarrasi, M., Reale, F., Peres, G. 2010, *ApJ*, 719, 576
- Handy, B. N. et al. 1999, *Sol. Phys.*, 187, 229
- Hansteen, V. H., Hara, H., De Pontieu, B., and Carlsson, M. 2010, *ApJ*, 718, 1070
- Hassler, Donald M., Rottman, Gary J., Orrall, Frank Q. 1991, *ApJ*, 371, 710

- Kamio, S., Hara, H., Watanabe, T., Fredvik, T., Hansteen, V. H. 2010, *Sol. Phys.*, 266, 209
- Klimchuk, J. A. 1987, *ApJ*, 323, 368
- Klimchuk, J. A. 2006, *Sol. Phys.*, 234, 41
- Klimchuk, J. A. 2009, *The Second Hinode Science Meeting: Beyond Discovery-Toward Understanding ASP Conference Series*, Vol. 415, proceedings of a meeting held 29 September through 3 October 2008 at the National Center for Atmospheric Research, Boulder, Colorado, USA. Edited by B. Lites, M. Cheung, T. Magara, J. Mariska, and K. Reeves. San Francisco: Astronomical Society of the Pacific, 2009, p.221
- Klimchuk, J. A., Karpen, J T., Antiochos, S. K. 2010, *ApJ*, 714, 1239
- Klimchuk, J. A., Patsourakos, S., and Cargill, P. J. 2008, *ApJ*, 682, 1351
- Lionello, R., Winebarger, A. R., Mok, Y., Linker, J. A., and Mikic, Z. 2012, *ApJ*, submitted
- Mariska, J. T., Boris, J. P. 1983, *ApJ*, 267, 409
- Marsch, E., Tian, H., Sun, J., Curdt, W., Wiegelmann, T. 2008, *ApJ*, 685, 1262
- Patsourakos, S., and Klimchuk, J. A. 2004, *ApJ*, 603, 322
- Patsourakos, S., and Klimchuk, J. A. 2006, *ApJ*, 647, 1452
- Peter, H., and Judge, P. G. 1999, *ApJ*, 522, 1148
- Scott, J. T. and Martens, P. C. H. 2012, *ApJ*, 742, 101
- Tripathi, D., Mason, H. E., Young, P. R. and Del Zanna, G. 2008, *A&A*, 481, 53
- Tripathi, D., Mason, H. E., Dwivedi, B. N., del Zanna, G., and Young, P. R. 2009, *ApJ*, 694, 1256
- Tripathi, D., Mason, H. E., Del Zanna, G. and Young, P. R. 2010, *A&A*, 518, 42
- Tripathi, D., Mason, H. E., Klimchuk, J. A. 2010, *ApJ*, 723, 713
- Tripathi, D., Klimchuk, J. A., Mason, H. E. 2011, *ApJ*, 740, 111
- Tripathi, D., Mason, H. E., Del Zanna, G. 2012, *ApJ*, in preparation
- Ugarte-Urra, I., Warren, H. P., Brooks, D. H. 2009, *ApJ*, 695, 642
- Viall, N. M., and Klimchuk, J. A. 2011, *ApJ*, 738, 24

- Viall, N. M., and Klimchuk, J. A. 2012, ApJ, arXiv:1202.4001
- Warren, H. P., Winebarger, A. R., and Mariska, J. T. 2003, ApJ, 593, 1174
- Warren, H. P. et al. 2008, ApJ, 677, 1395
- Warren, H. P., Winebarger, A. R., Brooks, D. H. 2010, ApJ, 711, 228
- Warren, H. P., Ugarte-Urra, I., Young, P. R., and Stenborg, G. 2011, ApJ, 727, 58
- Wilhelm, K.; Curdt, W.; Marsch, E.; et al. 1995, Sol. Phys., 162, 189
- Winebarger, A. R., Warren, H., van Ballegoijen, A., DeLuca, E., Golub, L. 2002, ApJ, 567, 89
- Winebarger, A. R., Warren, H P., Falconer, D. A. 2008, ApJ, 676, 672
- Winebarger, A. R., Schmelz, J. T.; Warren, H. P.; Saar, S. H.; Kashyap, V. L. 2011, ApJ, 740, 2
- Young, P. R., et al. 2007, PASJ, 59, 857
- Young, P. R., Watanabe, T., Hara, H. and Mariska, J. T. 2009, A&A, 587, 606
- Young, P. R., O'Dwyer, B., Mason, H. E. 2012, ApJ, 744, 14

Table 2: Mean, Median and Standard Deviation of the Doppler shift measured in moss regions and fraction of mossy pixels with definite Doppler shift.

Ion Name	log T_{max} (K)	Doppler shift in moss			$ v_i > 5$	$ v_i - \langle v \rangle > 5$
		Mean $\langle v \rangle$ km s ⁻¹	Median km s ⁻¹	Standard Deviation km s ⁻¹	(%)	(%)
Fe IX	5.85	-0.6	-1.7	4.9	31.0	28.7
Fe X	6.05	-0.6	-0.6	4.0	18.7	17.9
Fe XI	6.15	-1.4	-1.5	3.8	19.5	16.9
Fe XII	6.20	-0.1	0.9	3.7	16.0	16.0
Fe XIII	6.25	-2.3	-1.9	3.6	17.7	12.0

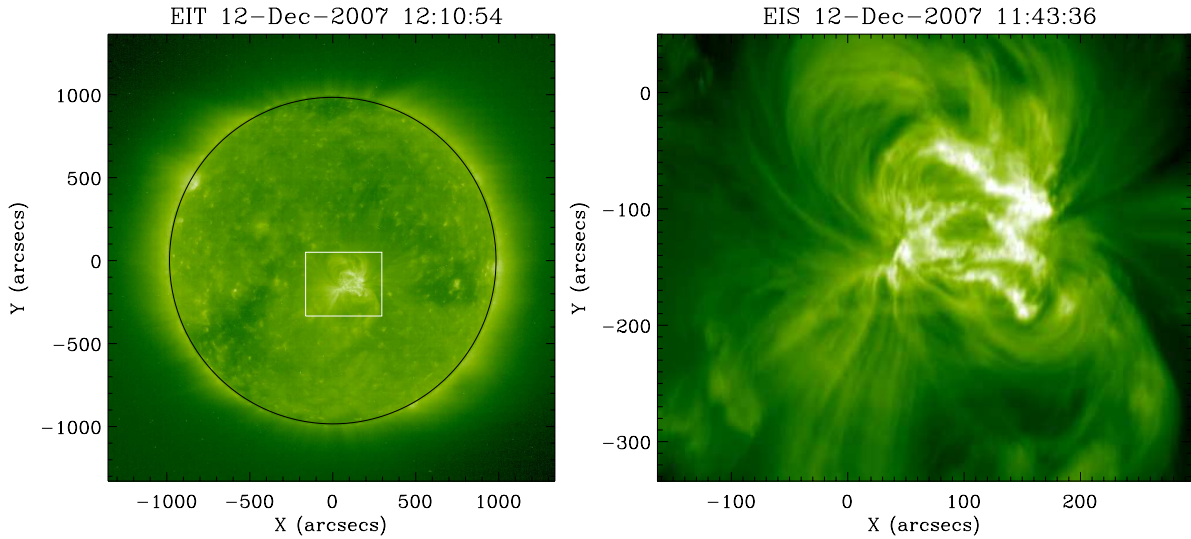


Fig. 1.— Left panel: Full disk image of the Sun recorded by the Extreme-ultraviolet Imaging Telescope (EIT) showing the active region located near the central meridian which was observed by the Extreme-ultraviolet Imaging Spectrometer (EIS). The over plotted box shows the region rastered by EIS. Right Panel: A monochromatic image built in Fe XII line using EIS observations corresponding to the box shown in the left panel.

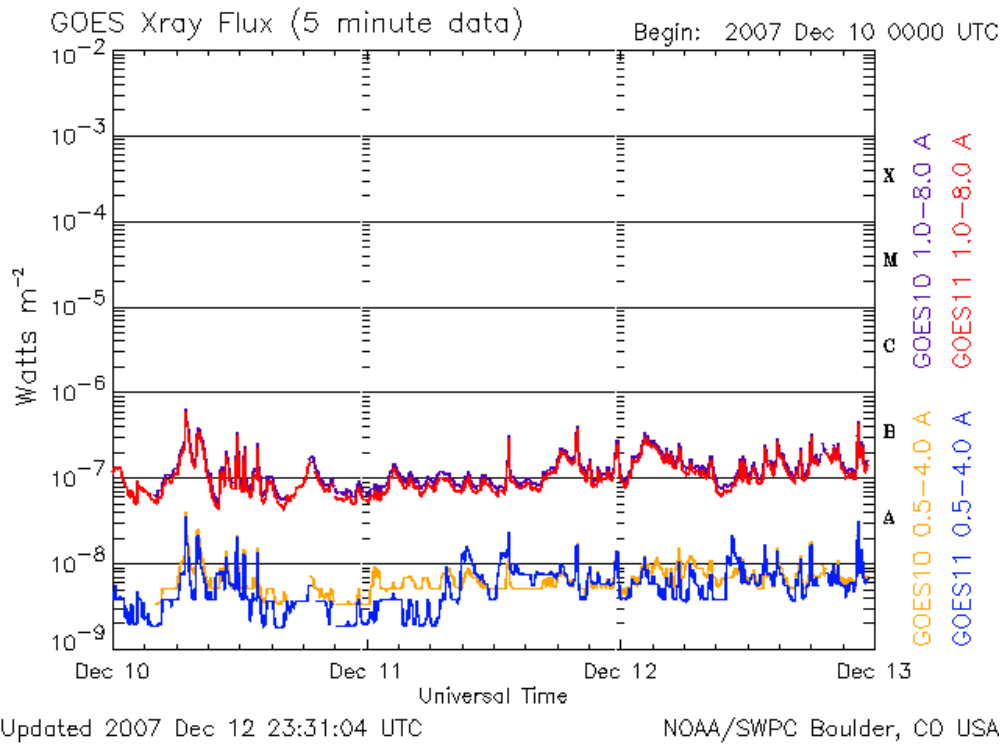


Fig. 2.— GOES X-ray flux profile from 2007 December 10 to 13, showing minimal activity.

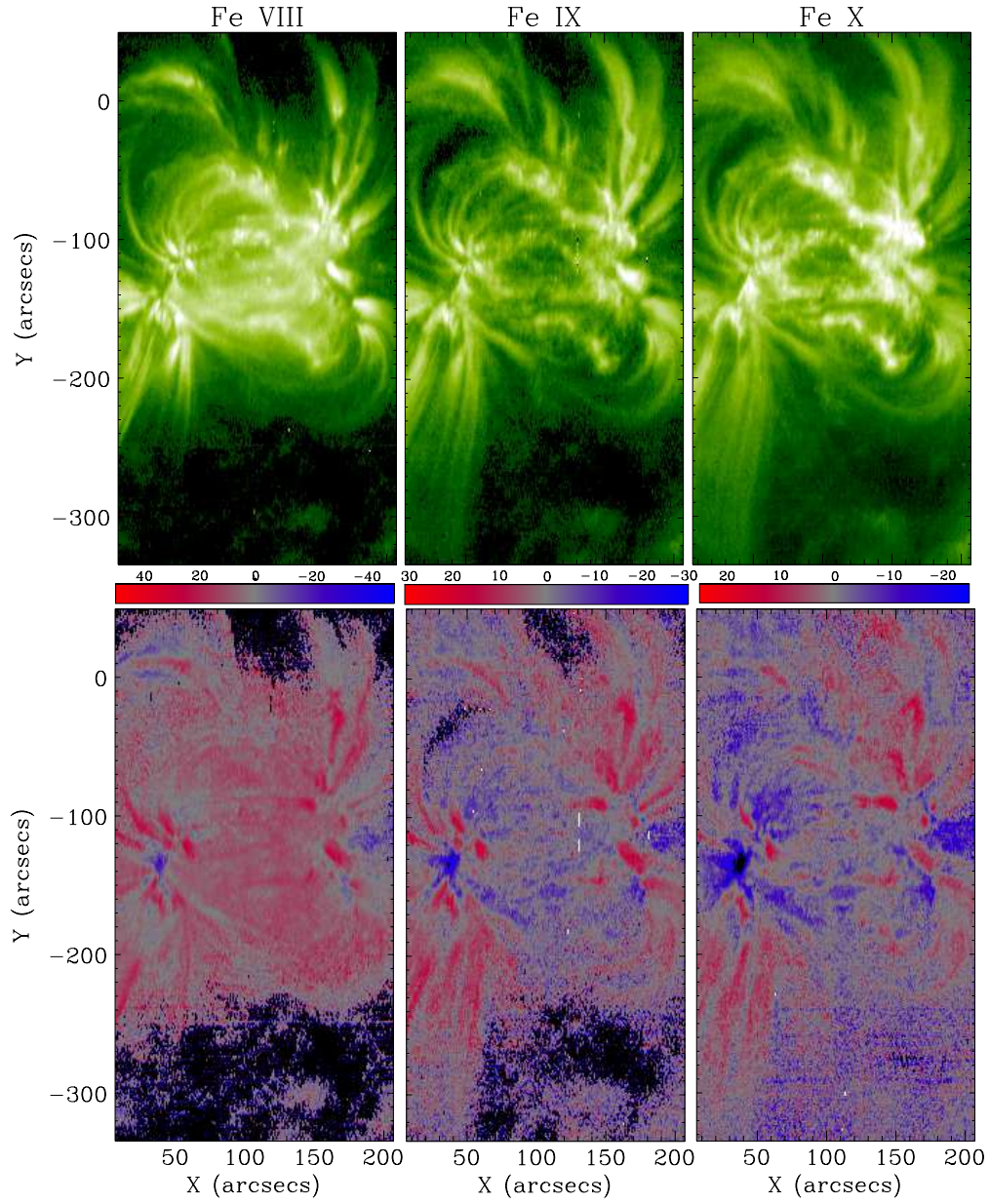


Fig. 3.— Intensity and Doppler maps derived in Fe VIII λ 186, Fe IX λ 197 and Fe X λ 184.

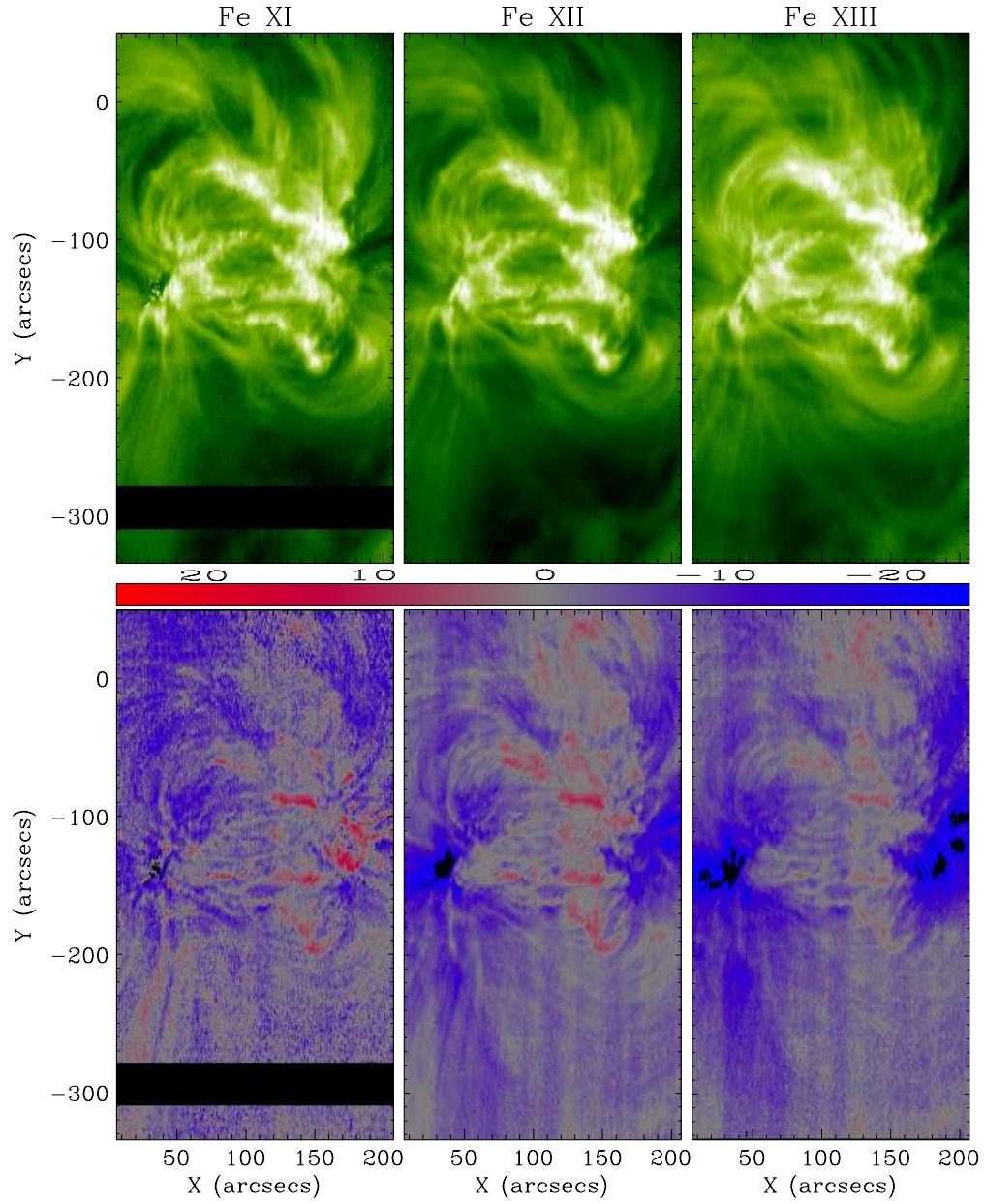


Fig. 4.— Intensity and Doppler maps derived in Fe XI λ 188.3, Fe XII λ 195 and Fe XIII λ 202.

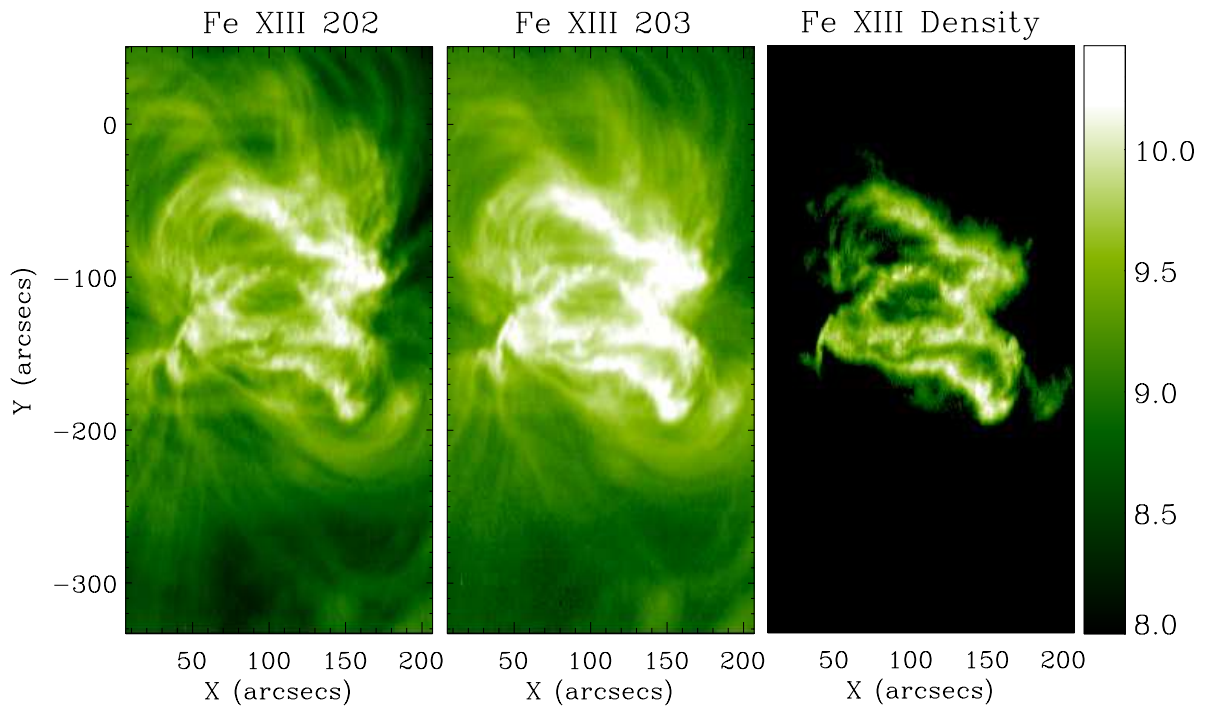


Fig. 5.— Left panel: Intensity image obtained in Fe XIII 202. Middle panel: Intensity image obtained in Fe XIII 203. Right panel: Density map using Fe XIII line ratios.

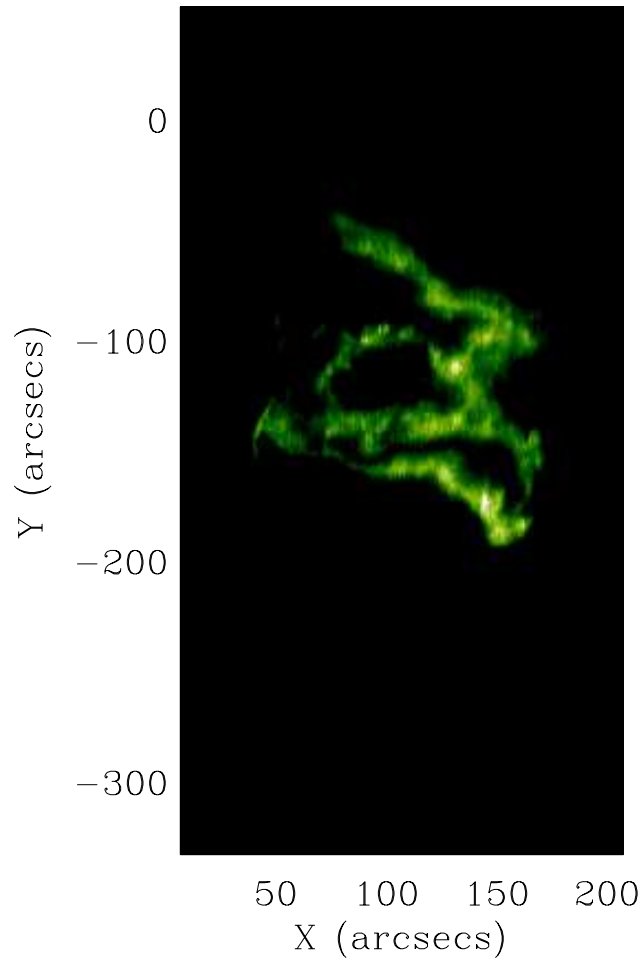


Fig. 6.— Fe XIII density map displayed with $\log N_e \geq 9.3 \text{ cm}^{-3}$.

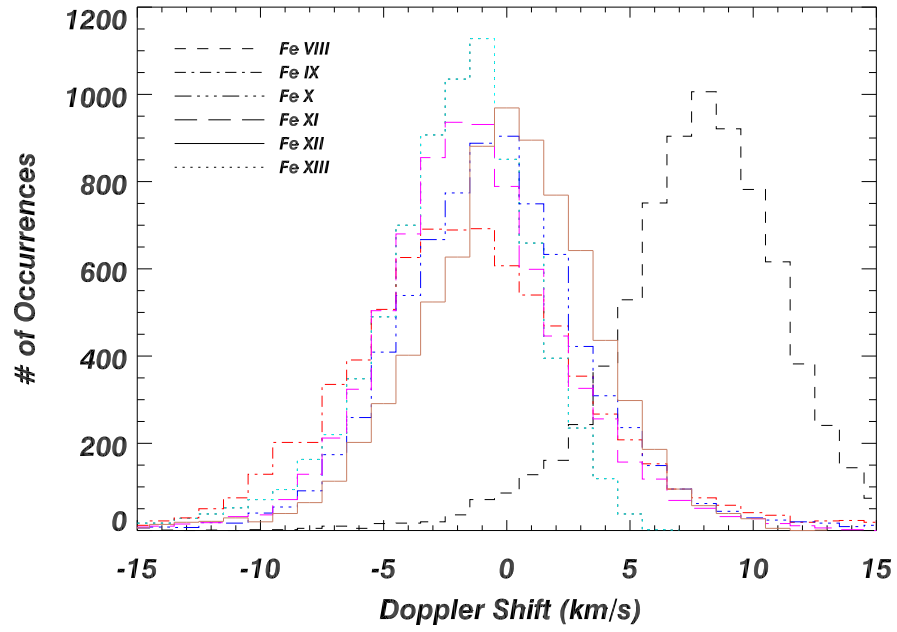


Fig. 7.— Histogram of the velocities corresponding to the pixels which have densities $\log N_e \geq 9.3 \text{ cm}^{-3}$.